Materials and Design 182 (2019) 108001

Contents lists available at ScienceDirect

Materials and Design

journal homepage: www.elsevier.com/locate/matdes

Impacts of process-induced porosity on material properties of copper made by binder jetting additive manufacturing

Ashwath Yegyan Kumar [a], Jue Wang [b], Yun Bai [a], Scott T. Huxtable [b], Christopher B. Williams [a,*]

[a] Design, Research, and Education for Additive Manufacturing Systems Lab, Virginia Tech Department of Mechanical Engineering, Blacksburg, VA 24061, USA
[b] Nanoscale Heat Transfer Lab, Virginia Tech Department of Mechanical Engineering, Blacksburg, VA, 24061, USA

HIGHLIGHTS

- The effects of powder configuration and process-induced porosity on material properties of binder jet copper were evaluated.
- Printed copper parts of 97% density featured 80 – 94% of wrought strength, thermal conductivity and electrical conductivity.
- Property variations with porosity were compared with models in the powder metallurgy and composite material literature.
- This work lays a foundation for the development of models for post-process-porosity-property relationships in binder jetting.

GRAPHICAL ABSTRACT

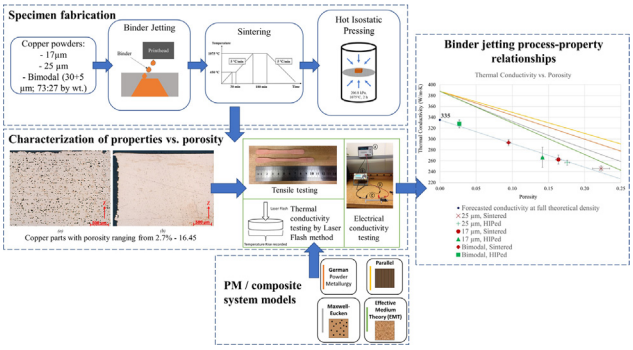

ARTICLE INFO

Article history:
Received 6 May 2019
Received in revised form 26 June 2019
Accepted 2 July 2019
Available online 03 July 2019

Keywords:
Binder jetting
Copper
Hot isostatic pressing
Powder metallurgy
Additive manufacturing
3D printing

ABSTRACT

Binder Jetting (BJ) is an efficient, economical, and scalable Additive Manufacturing (AM) technology that can be used in fabricating parts made of reflective and conductive materials like copper, which have applications in advanced thermal and electrical components. The primary challenge of BJ is in producing fully dense, homogeneous parts without infiltration. To this end, copper parts of porosities ranging from 2.7% to 16.4% were fabricated via BJ, by varying powder morphology, post-process sintering, and Hot Isostatic Pressing conditions. The aim of this study is to characterize and quantify the effects of porosity on the material properties of Binder Jet pure copper parts. Copper parts with the lowest porosity of 2.7% demonstrated a tensile strength of 176 MPa (80.2% of wrought strength), a thermal conductivity of 327.9 W/m·K (84.5% that of wrought copper), and an electrical conductivity of 5.6×10^7 S/m (96.6% IACS). The porosity-property relationship in these parts was compared against theoretical and empirical models in the literature for similar structures. These studies contribute towards developing a scientific understanding of the process-property-performance relationship in BJ of copper and other printed metals, which can help in tailoring materials and processing conditions to achieve desired properties.

1. Introduction

Copper is an important material with high thermal and electrical conductivities that can be used in applications involving enhanced heat transfer and electrical components. The layer-wise fabrication approach of Additive Manufacturing (AM) technologies can enable the

* Corresponding author at: 413E Goodwin Hall, 635 Prices Fork Rd, Blacksburg, VA 24061, USA.
E-mail address: cbwill@vt.edu (C.B. Williams).

https://doi.org/10.1016/j.matdes.2019.108001

fabrication of copper components that feature complex geometries, which could be leveraged in applications such as heat exchangers and rocket engine components with internal cooling channels [1]. However, copper's high thermal conductivity makes it difficult to control the melt pool if fabricating by laser- or electron beam-based Powder Bed Fusion (PBF) AM technologies, and its high reflectivity limits the choice of laser wavelengths that may be used [2]. Hence, processing pure, unalloyed copper powder using such systems can be challenging.

1.1. Additive manufacturing of pure copper

It has proven to be challenging to fabricate pure copper parts of sufficient densities via Laser PBF [3]. For example, Lykov and co-authors were able to achieve 88.1% density and a strength of only 149 MPa in copper parts fabricated using Selective Laser Melting (SLM) [4]. Other research has focused on special modifications to the laser technology [5,6] or machine and processing conditions [7] in order to circumvent said challenges. In comparison, researchers have been able to fabricate complex geometry copper parts via electron beam melting (EBM) such as auxetic structures [8] and parts with internal cooling channels [9]. Higher densities of up to 99.5% had been achieved by Lodes and co-authors [10], but they have yet to characterize the material properties. More recently, Guschlbauer and co-authors were able to fabricate nearly fully dense copper using selective electron beam melting (SEBM) with extremely high purity copper powder [11]. They developed process parameters for achieving thermal conductivity >385 W/m·K and electrical conductivity > 58 MS/m, provided a very low impurity content in the powder. While they were able to achieve superior mechanical properties along the build plane with a tensile strength of 177 N/mm^2 and an elongation at fracture of 59.3%, there was strong anisotropy as the parts tested perpendicular to the build plane (Z direction) were significantly weaker due to the presence of cracks.

By separating part creation from sintering, Binder Jetting (BJ) AM effectively circumvents the challenges faced by PBF AM technologies due to copper's high reflectivity and thermal conductivity. Specifically, BJ involves selectively jetting a binder into a copper powder bed to form a 'green' part in a layer-wise fashion (Fig. 1). Once printing is complete, the polymeric binder is cured in a low-temperature thermal post-process, which sufficiently improves part strength to enable depowdering. The green part is then placed into a furnace with a reducing atmosphere, in which the binder is pyrolyzed, and the copper powder is sintered and densified. While BJ offers benefits of scalability, efficiency, and the ability to process a wide array of materials, its primary disadvantage is its inability to fully densify the printed green parts without the infiltration of a secondary, lower-melting point material. This lack of densification is primarily due to (i) the process's inability to spread fine powders, and (ii) the powder bed's low density, which is due to the lack of compaction or agitation during layer recoating. The resultant parts' residual porosity causes deficiency in their final material properties. In the case of copper, BJ has been used to achieve up to 99.47% density through the use of optimized powder morphologies [12], printing parameters and sintering profiles [13], and post-process Hot Isostatic Pressing (HIP) [14]. Various intermediate densities achieved using different powders and post-processing conditions have been discussed elsewhere in the literature [15].

1.2. Research objective

The goal of this work is to lay a framework for developing process-structure-property relationships for BJ of copper, by mapping processing conditions to various material properties namely strength, ductility, and thermal and electrical conductivity. This is to be done by understanding the correlation between processing conditions and porosity and microstructure which has been explored elsewhere [15], and that between process-induced porosity and material properties. The latter is investigated in this article by analyzing the properties of specimens processed to achieve varying degrees of porosity. These properties are then compared to literature values in the context of porous copper prepared using powder metallurgy (PM), and to models for two-component systems with copper and the pores acting as each component.

A comparison with PM copper is appropriate since BJ is closest in nature to PM processes, albeit with loosely packed powders and no compaction. However, because of this difference between the processes, it has been seen that powder metallurgy knowledge does not directly translate to BJ. For instance, Bai and co-authors demonstrated that the use of bimodal powders in BJ yields higher density than when using small powders, which is contradictory to PM processes involving powder compaction, where finer powders are more favorable [12]. Similarly, two-component system-based models need not directly reflect Binder Jet part properties. These models are instead used in this study as a reference for comparison to BJ. The long-term goal is to use these models as a foundation to develop post-process-structure-property relationships specific to BJ.

An overview of the models used to study the measured properties is presented in Section 2, including mechanical properties (2.1), thermal and electrical conductivity (2.2), and the Wiedemann-Franz Law that provides a relationship between the two conductivities (2.3). The methods used to fabricate the specimens of varying porosity (3.1) and to test their tensile (3.2), thermal (3.3) and electrical conductivity (3.4) properties are presented in Section 3. The results from the analyses of strength (4.1), ductility (4.2), Young's modulus (4.3), thermal and electrical conductivities (4.4 and 4.5), and the Wiedemann-Franz Law (4.6) are reported in Section 4. Conclusions of the study and suggestions for future work are presented in Section 5.

2. Modeling porosity-property relationships

The models used in developing these porosity-property relationships are presented in this section.

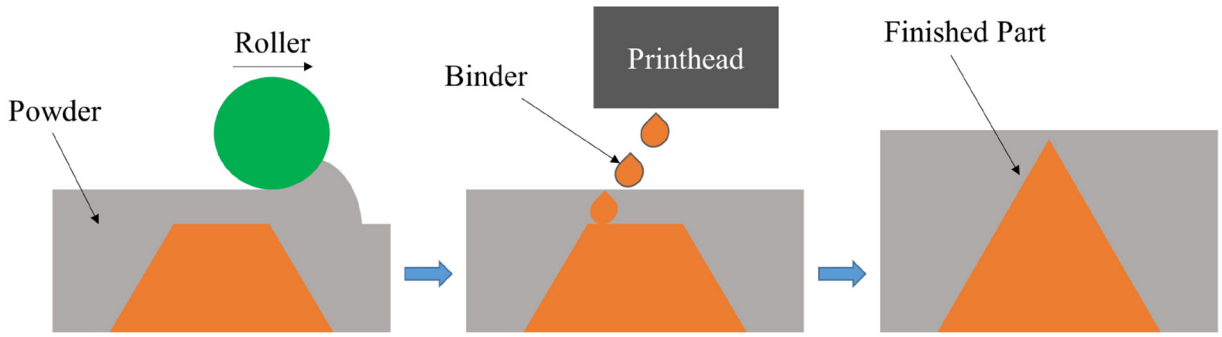

Fig. 1. Schematic diagram of the binder jetting process.

2.1. Mechanical properties

The tensile strength of porous PM specimens can be estimated to vary with density by Eq. (1), according to German [16]:

$$\sigma = \sigma_0 K \left(\frac{\rho}{\rho_t}\right)^m \tag{1}$$

where σ is the tensile strength of the porous material, σ_0 is the wrought strength of the same material (220 MPa for copper), and ρ and ρ_t are the density of the porous specimen and the theoretical density of the material, respectively. K is equivalent to a stress concentration factor due to the pores, and m is the exponential dependence of strength on porosity. Both parameters depend on the processing conditions, and the equation is valid in the absence of any microstructural problems. German also presents data on the strength of PM copper with various degrees of porosity in his book [16]. Upon fitting this data into Eq. (1), the values of parameters K and m were empirically found to be 0.9926 and 2.5150 respectively at an R^2 value of 0.9998.

Eq. (2) presents the dependence of ductility on porosity as proposed by Haynes [17]:

$$Z = \begin{cases} \dfrac{(1-\varepsilon)^{1.5}}{(1+c\varepsilon^2)^{0.5}}, \varepsilon<0.15, \dfrac{(1-\varepsilon)^{1.5}}{\left(1+0.15^2 c\right)^{0.5}}, \varepsilon>0.15 \end{cases} \tag{2}$$

where Z is the relative ductility (ratio of observed elongation of porous material to wrought material), ε is the porosity, and c is a coefficient representing the sensitivity of the ductility to porosity for the material under consideration. Fitting the ductility data provided by German [16] for various porosities under 15% into the model in Eq. (2), the value of c is obtained as 210.237, at an R^2 value of 0.9931. The elongation of wrought copper is taken as 0.45 based on the same data.

The mechanical property values observed in BJ copper samples are presented and discussed in Sections 4.1–4.4 in comparison with the above PM models.

2.2. Thermal and electrical conductivity

There are a number of models in the literature that describe the variation of thermal conductivity with porosity. A model proposed by Aivazov and Domashnev uses the following relation for the variation of thermal and electrical conductivity with porosity [18]:

$$k = k_0 \frac{1-\varepsilon}{1+n\varepsilon^2} \tag{3}$$

where k is the thermal conductivity of the porous specimen, k_0 is the thermal conductivity of pure wrought copper (388 W/m·K), ε is the porosity, and n is an experimentally determined constant. In regimes of porosity < 0.3, the relation may be approximated as follows [16]:

$$k = k_0(1-\omega\varepsilon) \tag{4}$$

where ω is a constant with a value between 1 and 2, also determined experimentally. ω of 1.136 for thermal conductivity and ω of 1.1228 for electrical conductivity were determined from German's experimental results, both having R^2 values of 0.9999. These values, although determined for copper fabricated from a different processing method, are taken as a reference to compare against the conductivity data obtained from Binder Jet copper.

Other models discussed in the literature [19–21] explore the effective conductivity from a physical perspective by modeling the porous material as a typical two-phase structure, and assuming various kinds of dispersions and shapes of one constituent (pores) with regard to the other (parent material). In all of the equations described below, k refers to the effective conductivity, k_1 and v_1 refer to the conductivity and volume fraction of the parent material (copper), and k_2 and v_2 to those of the dispersed medium (pores), respectively.

The Parallel model assumes that the phases are aligned parallel to the heat flow, providing alternating parallel conduction pathways. While this arrangement is not physically accurate for our samples, this model gives the upper bound to the effective thermal conductivity, as given by [22]:

$$k = k_1 v_1 + k_2 v_2 \tag{5}$$

The Maxwell-Eucken model assumes a distribution of non-interacting spherical pores within the copper medium, for which the effective thermal conductivity is given by [19]:

$$k = \frac{k_1 v_1 + k_2 v_2 \dfrac{3k_1}{2k_1+k_2}}{v_1 + v_2 \dfrac{3k_1}{2k_1+k_2}} \tag{6}$$

The Effective Medium Theory (EMT) model assumes a random distribution of two phases, for which the effective conductivity is given by [21]:

$$k = 0.25\left[(3v_2-1)k_2 + (2-3v_2)k_1 + \left\{[(3v_2-1)k_2 + (2-3v_2)k_1]^2 + 8k_1k_2\right\}\right]^{0.5} \tag{7}$$

A modified form of the EMT has also been proposed that takes into consideration grain boundary thermal resistance effects. The equation for this is as follows [21]:

$$k_{poly} = \left[\frac{1}{k_{single}} + nR_{th}\right]^{-1} \tag{8}$$

where k_{poly} is the thermal conductivity of the polycrystalline matrix, k_{single} is the thermal conductivity of pure, single crystal material in the absence of grain boundaries, n is the number of grain boundaries per unit length, and R_{th} is the thermal resistance of the grain boundaries.

The measured thermal and electrical conductivities of printed parts are compared against those predicted from Eqs. (4)–(7) and are presented in Sections 4.5 and 4.6. Additional analyses are done by using the observed thermal conductivity for each processing condition in the EMT and modified EMT models to calculate the conductivity of the copper matrix in each case, and further estimate the grain boundary thermal resistance, R_{th}, to compare to what is estimated in the literature [23,24]. These results are presented in Section 4.5.

2.3. Wiedemann-Franz law

The electrical and thermal conductivities of a metal are related by a semi-empirical relation called the Wiedemann-Franz Law, which is given by Eq. (9):

$$k = L\frac{T}{\rho} + b \tag{9}$$

where L is a constant called the Lorenz number, T is the absolute temperature, and ρ is the electrical resistivity. The quantities L and b represent the material-dependent electron and lattice (phonon) contributions to thermal conductivity, respectively. In the case of copper, previous literature has proposed the values of L and b to be 2.39×10^{-8} WΩ/K^2 and 0.075 W/m·K [25–27]. In their study of porous PM copper, Koh and Fortini determined L and b to be 2.307×10^{-8} WΩ/K^2 and 18.6 W/m·K, respectively [27].

One approach to a modification of the Wiedemann-Franz Law for the specific case of Binder Jet copper could be to fit the conductivity data to determine a modified equation [28]. However, in this study, the

observed thermal conductivity data is directly compared to predictions using Koh and Fortini's model for Oxygen-Free High Conductivity (OFHC) copper powders sintered to varying porosities [27]. They state that the constants are expected to be independent of porosity and dependent only on the material. It is assumed here that the difference in powder size and type, and the processing conditions in this study as compared to theirs, has a negligible effect on these constants. The results from this analysis are discussed in Section 4.7.

3. Experimental methods

3.1. Specimen fabrication

Fig. 2 shows a picture of the print bed during printing, indicating the layout of various specimens printed for testing. Due to build bed dimensional constraints, all samples were printed only in the XY orientation.

In previous work by the authors of this paper, different amounts of porosity have been achieved in BJ copper parts through the use of powders of different sizes and size blends, and post-process HIP [15]. A schematic diagram of the BJ process chain used in this work is presented in Fig. 3 and illustrates the process/post-process variables and control variables at each stage. Pure copper powders (obtained from ACuPowder Intl LLC) with median sizes of 17 μm, 25 μm, and a bimodal blend of powders with median sizes of 30 μm and 5 μm (mixed in the ratio of 73:27 by weight) were printed using an ExOne R2 system with a 70 μm layer thickness and 100% binder saturation. The binder used was the off-the-shelf binder from ExOne (PM-B-SR2–05) as it has previously been demonstrated to bind well with copper powders and leave minimal carbon residue upon pyrolysis [13]. Following the printing, all specimens were sintered as per the cycle shown in Fig. 3. This cycle incorporates a sintering temperature of 1075 °C for 3 h, after a 30-minute hold at 450 °C to allow for binder burn-off. All heating and cooling ramps are at a rate of 5 °C/min. Some of these sintered specimens were then HIPed at 1075 °C, 206.84 MPa (30,000 psi) for 2 h for analysis of HIPed specimens, and others retained for analyses of sintered specimens. From these varied parameters, specimens with six different amounts of porosity were thus achieved. The exact numbers of samples available for each characterization are presented in Table 1.

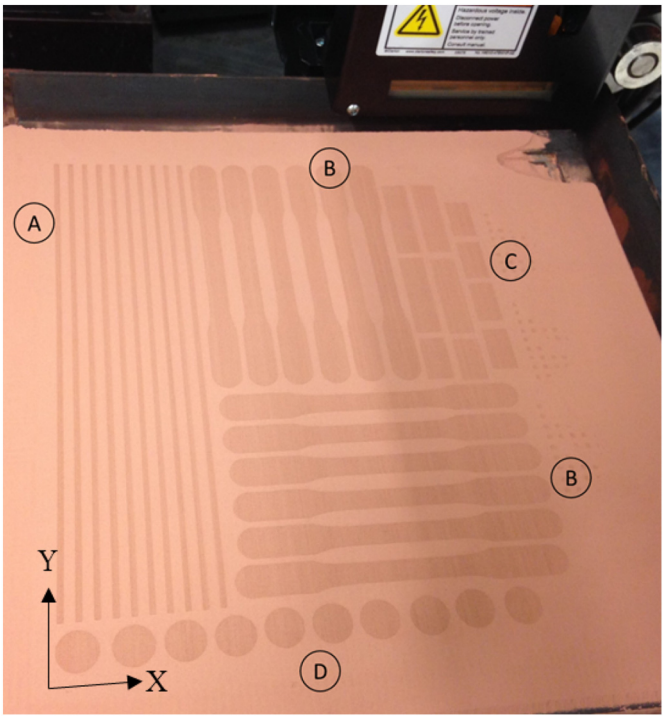

Fig. 2. Photograph depicting layout of parts in print bed: (A) Rods for electrical conductivity measurements, (B) Dogbones for tensile testing, (C) Rectangular coupons for density measurements, (D) Discs for thermal conductivity measurements.

3.2. Density, porosity, and microstructure

Density measurements were conducted via an Archimedes principle based apparatus to measure the mass of parts in air and in water and calculating the relative density. These specimens were oil impregnated, per the procedures outlined in the standard, for accuracy in measurements [29]. Optical porosity characterizations were done by polishing samples in successively finer grit papers and polishing cloths to remove scratches on the surface, and the samples were observed under an optical microscope. Three samples of each type were sectioned along all three planes for analysis. Polished samples were subsequently etched using nitric acid for microstructure characterization. The average grain size was determined using the Saltykov rectangle method [30,31]. For this method, rectangular sections were cropped from microscope images at random locations. For a given section of area A,the number of grains enclosed (n_{enc}) and those intercepted (n_{int}) by the perimeter of this rectangle were substituted into the equation for the number of grains per square millimeter, $N_A = (n_{enc} + 0.5n_{int} + 1)/A$. The average grain area was then calculated as $A_g = 1/N_A$, and the average diameter within the concerned section as the square root of A_g. These were then averaged across multiple sections. The key results of porosity and microstructure characterizations from previous work [15] by the authors are presented in Section 4.1 of this article.

3.3. Tensile testing

Tensile testing was carried out per the ASTM Standard E8/E8-M - 16a [32] using flat unmachined test specimens. The specimens were printed randomly in the XYZ or the YXZ orientations (Fig. 2) [33]. The tests were conducted with an INSTRON machine using a 50 kN load cell at a constant strain rate of 0.015 mm/mm/min per the recommendation in the standard (elongation rate of 0.381 mm/min) for a gauge length of 25.4 mm (1 in.). The ultimate tensile strength at break was measured, and the ductility is reported in terms of percentage elongation of gauge length.

3.4. Thermal conductivity measurement

The thermal conductivity of the specimens was calculated by the laser flash method, where the thermal conductivity is the product of thermal diffusivity, sample density, and specific heat. The procedures followed were based on the ASTM Standard E1461-13 [34]. The samples fabricated for these measurements were thin discs with diameters of 10 mm and thicknesses of ~2 mm (Fig. 2). A thin layer of graphite was sprayed onto the sample surfaces in order to enhance laser energy absorption and to avoid errors due to laser reflections.

In the laser flash method, a laser pulse is incident on the front surface of the disc, which creates a sudden rise in temperature at this surface. The thermal wave resulting from the laser pulse then diffuses through the sample, and it eventually creates a temperature rise on the backside of the sample. The temperature rise at the backside of the sample is recorded as a function of time and the maximum temperature rise (ΔT), along with the sample mass (m) and pulse energy from laser (ΔE), can be used to calculate the specific heat ($C_p = \frac{\Delta E}{m\Delta T}$). Additionally, the time required for the temperature at the backside to reach half of the maximum temperature rise, defined as half-rise time ($t_{1/2}$), along with the sample thickness (L), can be used to calculate the thermal diffusivity (α) from

$$\alpha = \frac{0.13879L^2}{t_{\frac{1}{2}}} \tag{10}$$

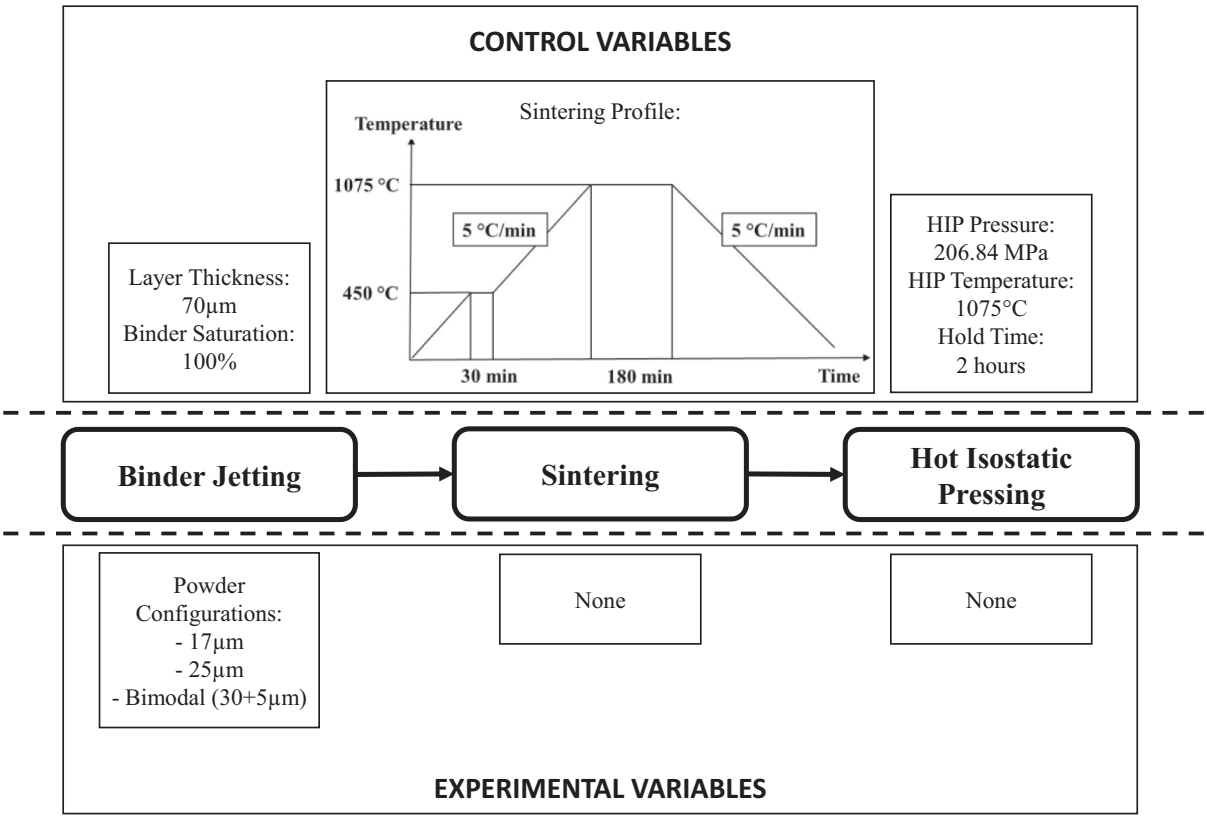

Fig. 3. Schematic diagram of the process chain.

The thermal conductivity (k) can then be calculated from

$$k = \alpha C_p \rho \tag{11}$$

where C_p is the specific heat capacity and ρ is the density of the specimen. Here, the specific heat was also measured using the laser flash method as mentioned previously, and the density was determined from Archimedes Principle based measurements (3.1).

3.5. Electrical resistivity measurement

The electrical resistivity of the samples was measured using a four-wire measurement apparatus. For this purpose, the samples printed were thin cylindrical rods (Fig. 2). A known current is passed through a measured length of the rod, and the corresponding drop in voltage is measured. The resistivity can be calculated from

$$\rho = \frac{R * A}{L} = \frac{V * A}{I * L} \tag{12}$$

where ρ is the resistivity, R is the resistance, V is the measured voltage drop, I is the known current, A is the cross sectional area, and L is the length of the rod.

Owing to the relatively low resistivity of copper, in order for the voltage to be measurable using the available multimeter, the length of the rod and the current passed through the rod had to be maximized, while the cross sectional area had to be minimal. Hence, a current of 10 A was passed using a high-current power source. Given the constraints of the printing process, and taking into account that the as-printed green parts must be able to withstand handling and depowdering prior to sintering, the parts were designed to have a diameter of 2 mm and a length of ~150 mm. Electrical conductivity values are presented either in S/m, or as a percentage of the International Annealed Copper Standard, or IACS (100% IACS = 5.8001×10^7 S/m).

4. Results and discussion

4.1. Characterizations of printed, sintered, and HIPed copper parts

The processing conditions used to obtain specimens of each density and the corresponding measured density and porosity are presented in Table 2. It is to be noted that while the maximum porosity achieved was 99.47% as indicated in Section 1.1, these results had been obtained for a limited set of trial specimens in a preliminary evaluation [15]. However, these results are not incorporated in this article as they were not repeatable owing to powder quality inconsistencies.

Table 1
Number of samples measured for each characterization.

Powder/processing condition		Density/porosity	Strength/ductility	Thermal conductivity	Electrical conductivity
25 µm	*Sintered*	5	3	5	4
	HIPed	5	3	5	5
17 µm	*Sintered*	5	3	5	4
	HIPed	5	4	5	5
Bimodal	*Sintered*	5	1	4	4
	HIPed	5	3	3	5

Table 2
Powders and processing conditions used to achieve different porosities.

Powder/processing condition		Density (% theoretical)	Porosity (%)	Avg. grain diameter (μm)	Ultimate tensile strength (MPa)	% elongation	Young's modulus (MPa)	Thermal conductivity (W/m·K)	Electrical conductivity ($\times 10^7$ S/m)
25 μm	Sintered	77.7 ± 1.2	22.3 ± 1.2	–	82.0 ± 5.3	28.9 ± 1.6	283.7 ± 24.2	245.7 ± 4.7	3.0 ± 0.1
	HIPed	82.4 ± 0.3	17.6 ± 0.3	24.1	129.3 ± 0.9	61.8 ± 2.3	209.2 ± 7.9	256.5 ± 4.4	3.7 ± 0.1
17 μm	Sintered	83.6 ± 0.4	16.4 ± 0.4	22.3	115.8 ± 9.2	48.5 ± 12.7	238.8 ± 65.3	262.3 ± 8.2	3.8 ± 0.4
	HIPed	85.8 ± 0.2	14.2 ± 0.2	34.0	135.3 ± 13.7	57.8 ± 12.3	234.1 ± 55.2	266.3 ± 18.5	3.7 ± 0.2
Bimodal	Sintered	90.5 ± 0.3	9.5 ± 0.3	13.4	144.9[a]	43.9[a]	330.1[a]	293.5 ± 5.5	4.7 ± 0.1
	HIPed	97.3 ± 0.1	2.7 ± 0.1	25.8	176.4 ± 6.5	67.2 ± 2.2	262.5 ± 13.0	327.9 ± 7.1	5.2 ± 0.1

[a] Only one sample measured.

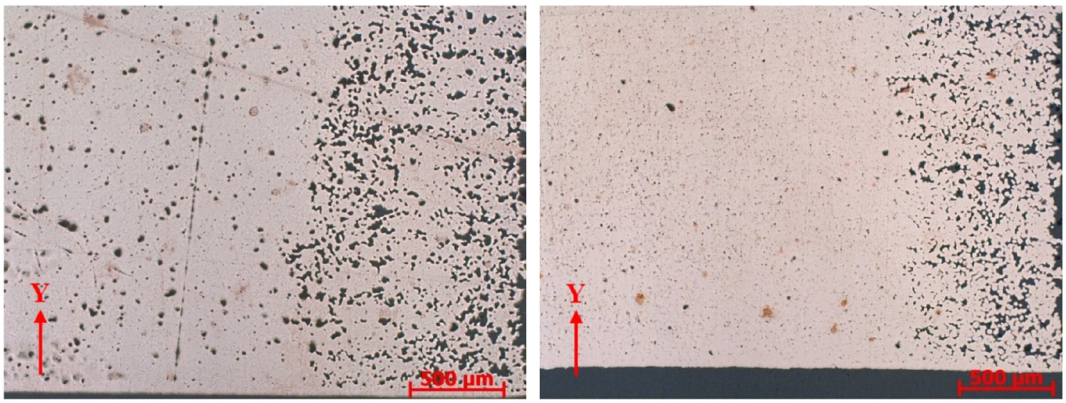

(a) (b)

Fig. 4. Porosity in 25 μm specimens (XY plane): (a) Sintered – 22.3%; (b) HIPed – 17.6%.

Some representative images of porosity observed in cross-sectional images of polished samples are provided in Fig. 4 (25 μm specimens), Fig. 5 (17 μm specimens) and Fig. 6 (bimodal specimens). The circular grey/black regions in these images are pores, while the straight, elongated artifacts are scratches resulting from damage during polishing. The micrographs indicate that the porosity distribution is heterogeneous in the case of 17 μm and 25 μm specimens, with more pores concentrated near the surface and between layers. Such a porosity distribution is different from those assumed in the models discussed in Section 2. In the case of bimodal parts, while the porosity distribution is more uniform, the processing conditions and powders result in microstructural issues that are not accounted for in these models. This limits the direct applicability of these models to BJ as discussed previously.

Upon etching these sections, equiaxed, twinned grains were observed in the micrographs of BJ printed and sintered specimens, which coarsened upon HIP. Fig. 7 provides representative images of the kinds of grain structure observed. Grain size measurement data are presented in Table 2, which evidence the grain coarsening observed. The 25 μm specimens contained extensive porosity and were not characterized for grain size.

4.2. Tensile strength

Fig. 8 compares the strength of the material obtained for each of the processing conditions to the values expected based on Eq. (1) (Section 2.1).

As expected, the strength increases with density. The highest tensile strength achieved is ~176 MPa at a density of 97.3%, which is 80.2% of the strength of wrought copper (220 MPa). It is evident that the tensile strength of both sintered and HIPed copper is below the value expected

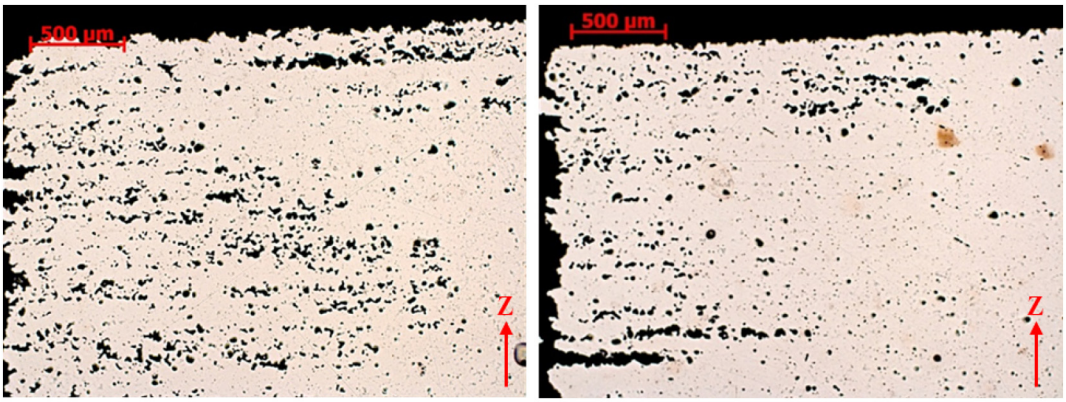

(a) (b)

Fig. 5. Porosity in 17 μm specimens (YZ plane): (a) Sintered – 16.4%; (b) HIPed – 14.2%.

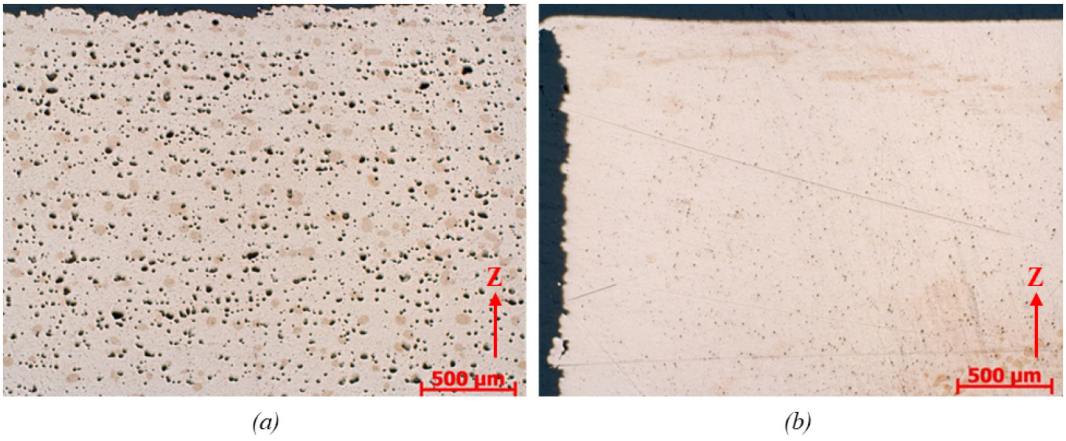

Fig. 6. Porosity in bimodal specimens (YZ Plane): (a) Sintered – 9.5%; (b) HIPed – 2.7%.

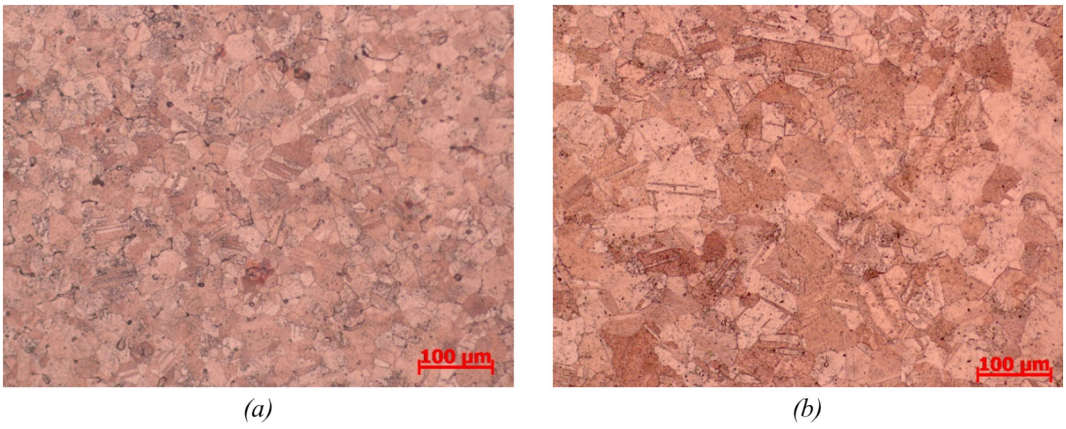

Fig. 7. Representative micrographs – (a) Sintered and (b) HIPed bimodal (30 + 5 µm) specimens.

based on the model. The disparity may be due to microstructural differences caused by the difference in powder types and processing conditions as compared to those used to construct the PM model, as the parameters K and m in Eq. (1) are dependent on the processing conditions and grain structure among other factors. However, the authors were unable to access the details of the processing conditions used and the microstructures obtained for PM copper used to develop this model [15], which limits the ability to make precise scientific

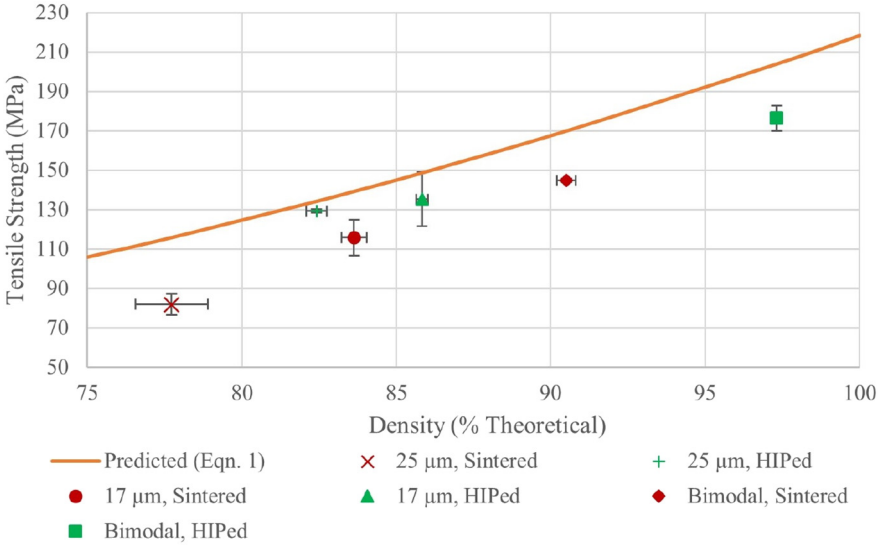

Fig. 8. Tensile strength observed in comparison to model predictions.

comments on this disparity. The powder size can dictate the grain sizes in the sintered parts, and HIP can further recrystallize or coarsen each of these (Section 4.1). A detailed evaluation of the grain structures and nature of porosity in the sintered, as well as HIPed, samples using 3-dimensional visualization techniques may provide further insight into the significance of these findings in the context of PM data for similar powders. An Energy Dispersive Spectrometry (EDS) study of the surface composition of BJ copper has shown the presence of residual carbon of up to 4.69 wt% after pyrolysis of binder after sintering as presented by Bai and co-author in a previous study [35]. This can also be a detriment to the strength. Future studies may also consider the influence of printing orientation rather than randomizing the orientations as in this study, as this may provide further information regarding the isotropy of strength of parts fabricated using this process chain.

4.3. Ductility

Fig. 9 presents the ductility of the fabricated specimen along with the predicted values based on the model given in Eq. (2). It is important to note that one may expect limited repeatability in the results for 25 μm sintered specimens and bimodal sintered specimens due to (i) defects in samples from damage caused by impurities in the powder, (ii) damage to green parts while handling, and (iii) the availability of only one bimodal sintered sample for testing.

The printed parts have higher ductility than the values expected from the model in the case of the 17 μm and 25 μm parts (~15% and higher porosity), while the model seems to overpredict the ductility in the case of bimodal parts (<10% porosity). In the case of parts with open porosity (>~10%), this could be due to the distribution of porosity localized near the surface as compared to the internal regions, and layer interface bonding defects in binder jet parts as seen in the sample micrographs of 17 μm specimens in the YZ plane (Fig. 5). This pore distribution is different from the uniform spread of pores that may be expected from sintered powders, as assumed in the model.

In the case of lower porosity (i.e., bimodal) parts, the surface porosity is completely sealed, with the majority of the remaining porosity homogeneously distributed in the inner regions (Fig. 6). This porosity distribution may be closer to what is obtained by sintering of loose powders to similar densities, and the difference in ductility may be due to factors such as difference in grain structure, purity of the copper powders used in each case, and oxide formation resulting from binder burn-off (as discussed in [35]). A detailed experimental design to study the influence of these factors is required to draw precise comparisons between PM techniques and the BJ-sintering-HIP processing methodology. Such detailed investigations in the future can help formulate more accurate mathematical relations to express the variation of ductility with porosity for these processing conditions.

4.4. Young's modulus

The Young's modulus is expected to decrease with increase in density per German's data for PM copper [16]. From Table 2, it is observed that it does decrease upon densification of the 25 μm and bimodal powder specimens, but there is no statistically significant reduction for 17 μm specimens as the density difference upon HIP in that case is also minimal. A relation similar to Eq. (1) may be expected for the dependence of Young's modulus on porosity as well for PM copper. Using the data in [16], the values for K and m were found to be 1.0092 and −3.83 respectively at an R^2 value of 0.9987. However, this relation does not seem to apply in a comparison of, say, high porosity 25 μm specimens vs. low porosity bimodal specimens. This is supported by discussions in [36,37]. These works suggest in their analysis of Young's modulus-porosity correlations that the parameters K and m can be strongly dependent on the pore structure and processing conditions, and that this dependency can vary from one property to another. They present that this is not understood thoroughly enough for an objective micromechanical determination of pore characteristics using the empirically determined values of these parameters. These may hence be further explored in future work by an independent analysis of pore structures in addition to empirical calculations.

Further, there are more involved micromechanical models in the two-component systems literature for Young's modulus including those based on Maxwell's work [38,39] and Mori and Tanaka's work [40] that can potentially be applied to BJ copper, with the assistance of further understanding of pore geometry from three-dimensional visualization tools such as Computed Tomography (CT) scans. This is left to be part of future studies, with the focus of this article being kept on thermal and electrical conductivity models for copper in the following sections. There is also prior work on models developed for Young's modulus of BJ ceramics [36] that can form as a suitable reference for the development of similar models for metals such as copper.

4.5. Thermal conductivity

The results from thermal conductivity measurements conducted with the laser flash method are presented in Fig. 10 along with a comparison to the various models introduced in Section 2.2.

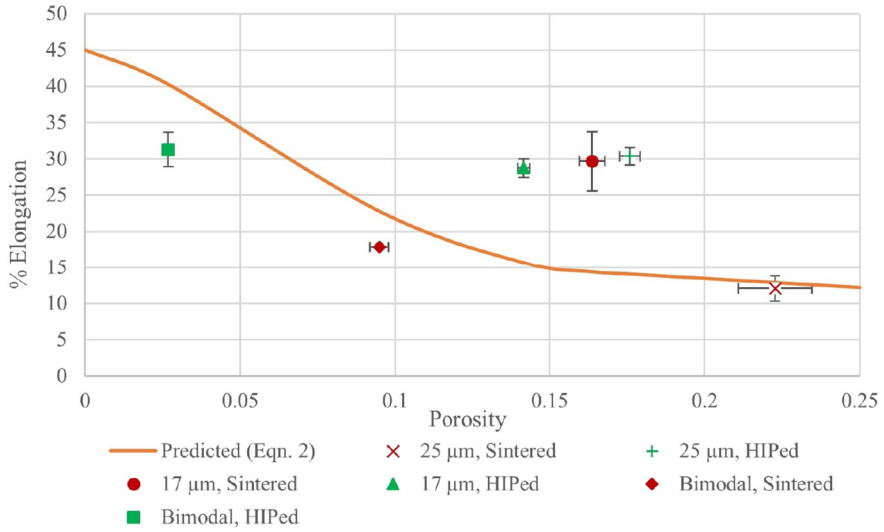

Fig. 9. Ductility observed in comparison to model predictions.

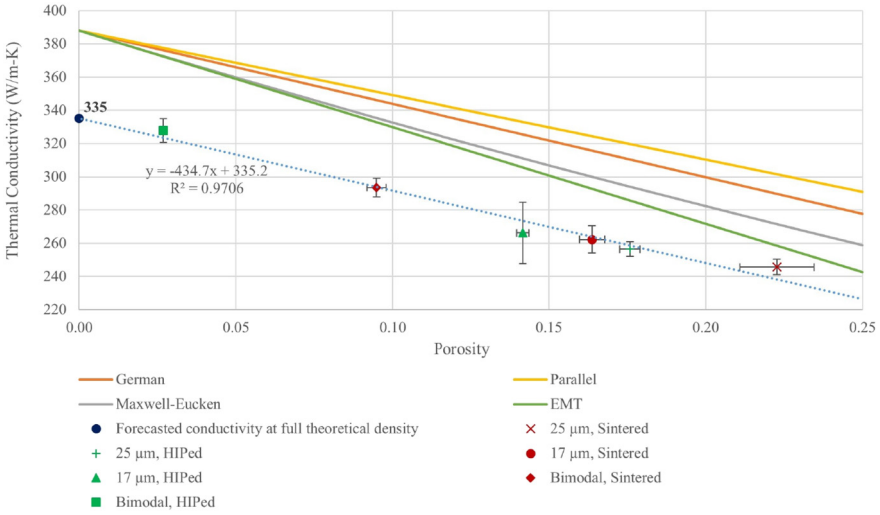

Fig. 10. Thermal Conductivity observed in comparison to model predictions.

The thermal conductivity increases with decrease in the porosity, as is expected. A highest conductivity of 327.9 W/m·K is obtained with bimodal HIPed specimens, which is 84.5% of the theoretical conductivity (388 W/m·K). It is clear in Fig. 9 that all of the models overestimate the conductivity in comparison to the observed data. There are several possible reasons for the low thermal conductivity values observed in the samples. First, there is a disparity in the shapes and distribution of the pores assumed in comparison to each of the models, as explained in Section 2.2, thus the models do not accurately represent the physical conditions of the samples. In addition, none of the models account for the presence of grain boundaries or microscale defects within the samples, both of which have the effect of reducing thermal conductivity.

While the measured thermal conductivity is lower than expected from the models, the thermal conductivity does scale nearly linearly with porosity as predicted by the models. Extrapolating from the data gives a value of thermal conductivity for fully dense parts to be ~335 W/m·K. This value is about 14% lower than the expected thermal conductivity (388 W/m·K) for pure copper. While this extrapolation is not to be taken as an accurate scientific prediction for the thermal conductivity of fully-dense BJ parts, it is presented to note that the expected value will be less than that of pure copper processed via traditional PM of fine powders. This reduction in thermal conductivity can be attributed to possible impurity of the copper powders used, residual carbon after the binder burn-off, and the presence of thermal resistance at the grain boundaries. These aspects may be individually investigated in depth in future work.

An alternate approach to examining the thermal conductivity of copper is to use the effective medium theory (EMT, Eq. (7)). With the EMT one can obtain a better approximation of the thermal conductivity of the solid copper within the matrix (k_1) by rewriting Eq. (7) in the following form.

$$k_1 = \frac{2k^2 + (v_1 - 2v_2)k_2 k}{2v_1 k + k_2 - v_2 k} \tag{13}$$

Again, here k is the thermal conductivity of the porous sample, k_1 and v_1 are the thermal conductivity and volume fraction, respectively, for the solid copper, and k_2 and v_2 are the thermal conductivity and volume fraction, respectively, for the voids in the samples. This expression returns the conductivity (k_1) of the pore-free copper matrix for each processing condition, accounting for the effects of grain boundaries, impurities, and any other non-porosity-related effects. This calculated value of k_1 will henceforth be referred to as k_{fd}, for conductivity at "full density" for a given powder and processing condition combination. Fig. 11 below plots the value of k_{fd} calculated for each of the processing conditions.

This plot shows that for all of the cases, the estimated thermal conductivity of the pore-free copper matrix is at least 335 W/m·K.

The next step in attempting to understand the physics of heat conduction in copper processed in this manner is to calculate the grain boundary thermal resistance for the samples in this study. This analysis excludes the data from sintered 25 µm specimens, since their microstructure could not be characterized due to extensive porosity. The anomalous prediction for high thermal conductivity as seen in Fig. 11 could hence not be scientifically explored further than the possible inapplicability of this model to specimens with porosity that is extensive as well as highly heterogeneous. The thermal resistance due to grain boundaries can be estimated with Eq. (8) and by replacing the thermal conductivity of the polycrystalline material (k_{poly}) with the measured value of the fully dense copper matrix (k_{fd}) as

$$K_{poly} = k_{fd} = \left[\frac{1}{k_{single}} + nR_{th}\right]^{-1}. \tag{14}$$

The number of grain boundaries per unit length (n) is estimated based on the grain size data from Table 2. The grain size is averaged over both orientations for each type of specimen. The total number of grains per unit length is approximated as being equal to the total length

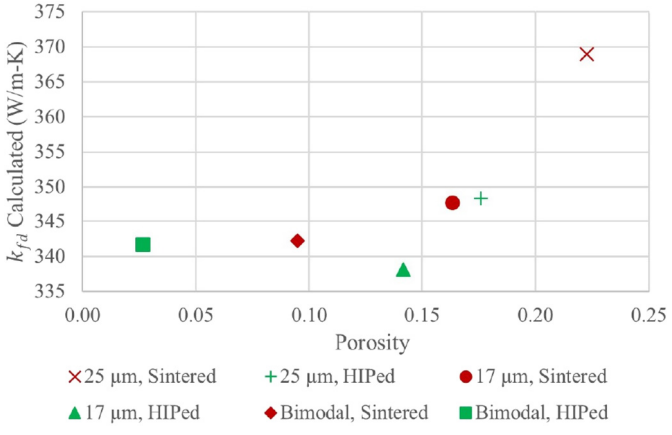

Fig. 11. Thermal conductivity at full density (k_{fd}) calculated for each processing condition.

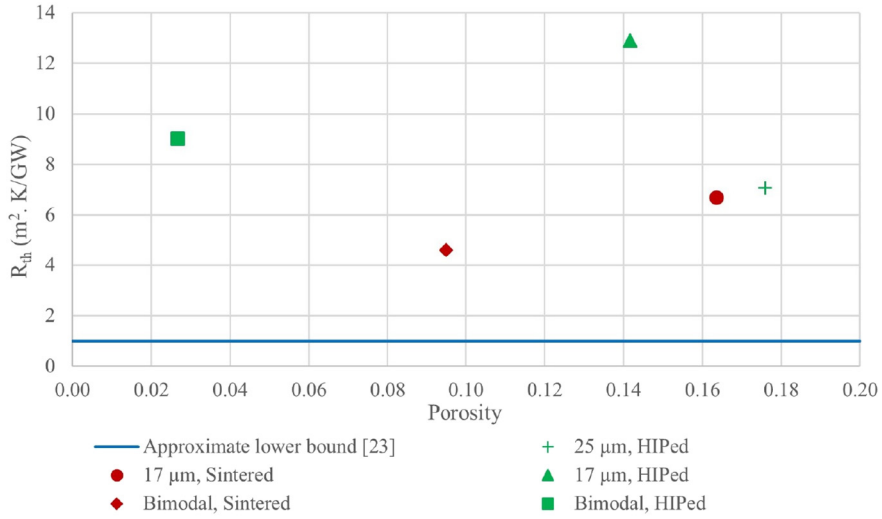

Fig. 12. Grain boundary thermal resistance estimated from the modified EMT model. The blue line represents an approximate lower bound for the thermal resistance for metal-metal interfaces from measurements done by Gundrum et al. [23]. (For interpretation of the references to colour in this figure legend, the reader is referred to the web version of this article.)

(1 m) divided by the average grain diameter, d_g (in meters). Rearranging Eq. (14) for R_{th} yields

$$R_{th} = \frac{1}{n}\left(\frac{1}{k_{fd}} - \frac{1}{k_{single}}\right), \tag{15}$$

where k_{single} is taken as 388 W/m·K. The results of calculating the grain boundary thermal resistance for each processing condition are presented Fig. 12.

The data shows that the thermal resistance of grain boundaries in the cases of Binder Jet copper subjected to sintering/HIP is within an order of magnitude of the lower bound that one could expect for metal-metal interfaces as demonstrated in the literature [23,24]. One would reasonably expect that the boundary resistances here would be greater than for the pristine metal-metal interfaces that give the lower bound, since these samples are far from ideal as they include impurities, carbon residue, and oxides among other factors.

4.6. Electrical conductivity

A similar analysis is done for the electrical resistivity measurements to compare with the same set of models as in Section 4.5, and the results are presented in Fig. 13.

The electrical conductivity follows a trend similar to that reported for the thermal conductivity prediction. The conductivity of HIPed bimodal specimens was observed to be 5.2×10^7 S/m (93.6% IACS). However, the electrical conductivity prediction at full density approaches a value of 5.6×10^7 S/m (or 96.6% IACS), which is closer to the theoretical value of 5.8×10^7 S/m (100% IACS) than the thermal conductivity projection (86.4%). However, it is important to note that the electrical and thermal conductivities were not measured in the same directions with respect to printing orientations. Specifically, the electrical conductivity specimens were all rods printed parallel to the build plane on the printer (XYZ orientation, per [33]), with the measurements taken along the length (Y-direction). The thermal conductivity specimens were discs printed with the thickness along the build direction (XYZ orientation), which is the direction of measurement (Z-direction). Hence, layer interface bonding issues in the higher-porosity specimens (Figs. 4,5) may cause disparity in these values. This difference is further investigated in Section 4.7 using the Wiedemann-Franz Law.

4.7. Relation between thermal and electrical conductivity

The thermal conductivity measured for various porosities is plotted against that calculated by the Wiedemann-Franz Law as described by Koh and Fortini for PM copper (Section 2.3) in Fig. 14.

The figure shows that the model underestimates the thermal conductivity for higher porosity (lower electrical conductivity) specimens and overestimates it for lower porosity specimens. Since the thermal transport through the metallic copper is dominated by the electronic contribution, the Wiedemann-Franz law should be applicable. However, since the parts do exhibit directional porosity (layer bonding defects in higher porosity specimens) and the measurements of thermal and electrical conductivity were taken in orthogonal directions, it is likely that this anisotropy is the reason for the variation between the model and the experimental results.

5. Summary and future work

The effects of porosity on various material properties of copper fabricated by BJ of three different powder types, followed by sintering and HIP, have been investigated in comparison to models in the literature for copper parts with porosity achieved through other processing methods. The major findings are summarized below:

- The bimodal, HIPed copper specimens were found to have the highest density of 97.3%. These also had the most favorable material properties, of tensile strength of 176 MPa (80.2% wrought strength), thermal conductivity of 327.9 W/m·K (84.5% of wrought value), and an electrical conductivity of 5.2×10^7 S/m (93.6% IACS).
- The strength of copper parts is found to be less than that predicted by the model (Fig. 8), which may be attributed to the presence of microstructural issues and differences in the grain structure due to differences in powder material and/or manufacturing techniques.
- The ductility model overestimates the elongation in the low-porosity regimes due to microstructural and compositional differences, and underestimate the same in the high-porosity regimes where the porosity spread is localized to the surface as compared to uniformly distributed pores in sintered Cu powders (Fig. 9).
- The measured thermal conductivity was found to decrease linearly with increasing porosity, and it was also ~10–15% less than that predicted by various models in the literature (Fig. 10). The reduced thermal conductivity was attributed to thermal resistance possibly introduced through grain boundaries, defects created during the manufacturing process, carbon residue from binder pyrolysis, or the presence of oxides.

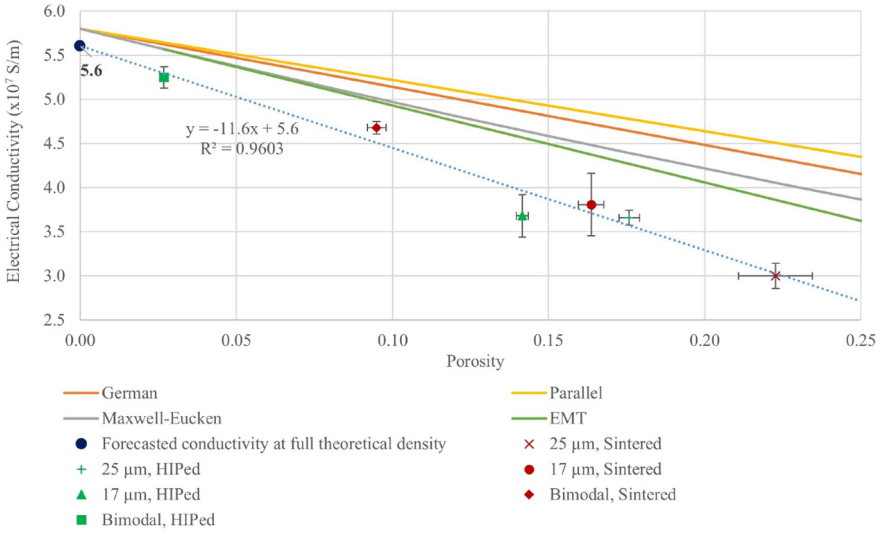

Fig. 13. Electrical conductivity observed in comparison to model predictions.

- The Effective Medium model gave the best predictions of the thermal conductivity (Fig. 11), and this model was also useful for estimating an upper limit on the grain boundary thermal resistance (Fig. 12).
- The electrical conductivity was found to compare similarly with models existing in the literature. The prediction for electrical conductivity at full density, based on a generalized linear trend, is 96.6% IACS (Fig. 13). Using these electrical conductivity values to estimate the thermal conductivity with the Wiedemann-Franz Law gave a variation in the disparity between the predicted and observed thermal conductivity (Fig. 14). These differences are likely due to the fact that the electrical and thermal conductivity were measured in perpendicular directions, and the samples were not isotropic (Figs. 4, 5).

In general, the properties analyzed are observed to consistently fall below the predictions based on both Powder Metallurgy and two-component structural models. In the case of a comparison with PM copper, differences are attributed to the less uniform porosity distribution, variations in purity of powders, and in grain structures arising from various powders and processing conditions for each level of porosity achieved using BJ. A more elaborate analysis of achieving varying degrees of porosities through changing the sintering or HIP conditions for each of the powders is required to derive relations similar to PM equations (Section 2) for BJ. The predictions for thermal and electrical conductivity based on models for two-component systems are also higher than the observed values, due to (i) each of these models assuming a different kind of porosity distribution than that observed for each of the Binder Jet specimens, and (ii) the possibility of additional thermal resistances in the samples due to grain boundaries, impurities, or other defects. Better approximations for both the porosity distribution (CT scans) and the influence of grain boundary effects and various impurities (composition analysis for each kind of specimen) can help to develop accurate, physics-based two-component models for thermal and electrical conductivity predictions in the future. While in this article, the authors' primary focus has been on the thermal and electrical conductivity as properties of interest, an analysis of the Young's modulus of specimens of different porosities may be placed in the context of related models in the PM and 2-component systems literature in future work. This can provide for a clearer understanding of the elastic

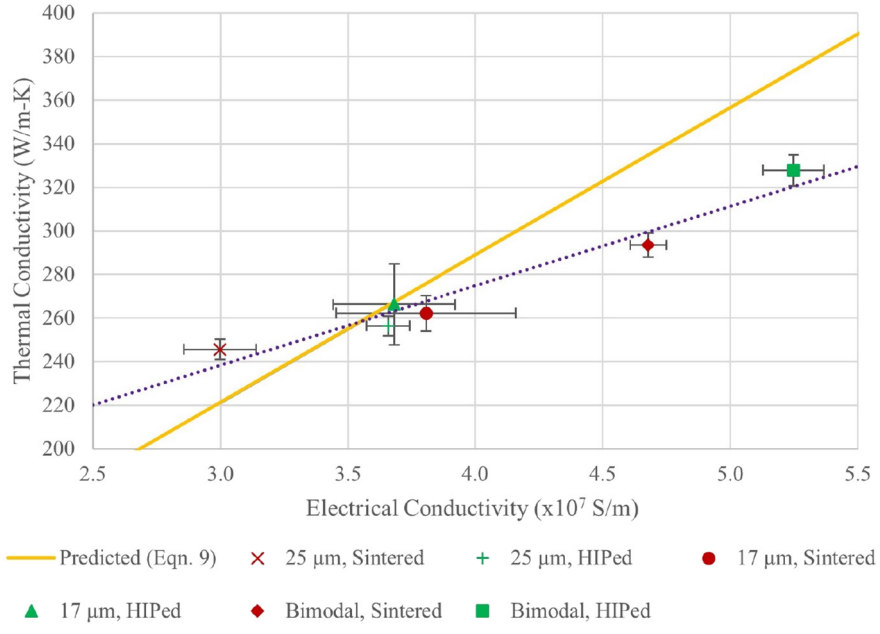

Fig. 14. Observed thermal conductivity in comparison with that calculated using the Wiedemann-Franz Law.

properties, as discussed in Section 4.4. Additionally, it may be worth investigating the scalability of these material properties with increasing size and geometrical complexity of samples, owing to the unique layer-dependent nature of porosity in these specimens.

This study has placed the results for BJ of copper within the context of theoretical models in the powder metallurgy and two-component systems literature. This line of work presents opportunities for future studies incorporating statistical design of experiments to perform further investigations of the effects of powder types, printing orientation, processing parameters, measurement directions, and the development of specialized models for the BJ process chain. Developing such models will enable one to print copper parts of desired material properties using BJ by adjusting the material and processing parameters to achieve the corresponding degree and type of porosity.

Data availability

The raw/processed data required to reproduce these findings cannot be shared at this time as the data also forms part of an ongoing study.

CRediT authorship contribution statement

Ashwath Yegyan Kumar: Conceptualization, Methodology, Formal analysis, Investigation, Data curation, Writing - original draft, Visualization. **Jue Wang:**Methodology, Formal analysis, Investigation, Visualization. **Yun Bai:**Conceptualization, Investigation. **Scott T. Huxtable:** Conceptualization, Methodology, Validation, Formal analysis, Resources, Writing - review & editing, Visualization, Supervision. **Christopher B. Williams:**Conceptualization, Methodology, Validation, Resources, Data curation, Writing - review & editing, Visualization, Supervision, Project administration, Funding acquisition.

Acknowledgements

This material is based upon work supported by the National Science Foundation [grant number CMMI #1254287]. The authors acknowledge technical support provided by the ExOne Co. The authors acknowledge Dr. Anders Eklund of Quintus Technologies for their contributions regarding HIP parameter selection. Robert Mills (Virginia Tech EXTREME Lab) is acknowledged for his assistance in sample preparation. Matthew Meeder and Dr. Al Wicks (Department of Mechanical Engineering, Virginia Tech) are acknowledged for their contributions in conducting preliminary studies on conductivity - porosity variations in Binder Jetting.

References

[1] T. McMahan, NASA 3-D Prints First Full-Scale Copper Rocket Engine Part, NASA Press Off, 2015https://www.nasa.gov/marshall/news/nasa-3-D-prints-first-full-scale-copper-rocket-engine-part.html, Accessed date: 9 June 2019.
[2] F. Sciammarella, M.J. Gonser, M. Styrcula, Laser additive manufacturing of pure copper, SME RAPID Conference and Exposition, 2013 , Pittsburgh, PA https://www.researchgate.net/publication/282266869_Laser_Additive_Manufacturing_of_Pure_Copper.
[3] S.R. Pogson, P. Fox, C.J. Sutcliffe, W. O'Neill, The production of copper parts using DMLR, Rapid Prototyp. J. 9 (2003) 334–343, https://doi.org/10.1108/13552540310502239.
[4] P.A. Lykov, E.V. Safonov, A.M. Akhmedianov, Selective laser melting of copper, Mater. Sci. Forum 843 (2016) 284–288, https://doi.org/10.4028/www.scientific.net/MSF.843.284.
[5] L. Kaden, G. Matthäus, T. Ullsperger, H. Engelhardt, M. Rettenmayr, A. Tünnermann, S. Nolte, Selective laser melting of copper using ultrashort laser pulses, Appl. Phys. A Mater. Sci. Process. 123 (2017), 596. https://doi.org/10.1007/s00339-017-1189-6.
[6] Green Light for New 3D Printing Process - Fraunhofer ILT, (n.d.). https://www.ilt.fraunhofer.de/en/press/press-releases/press-release-2017/press-release-2017-08-30.html [Accessed June 9, 2019].
[7] Revolutionising Copper through Additive Manufacturing _ 3T-am, (n.d.). https://www.3t-am.com/news/revolutionising-copper-through-additive-manufacturing?from=3trpd.co.uk [Accessed June 9, 2019].
[8] L. Yang, O. Harrysson, H. West II, D. Cormier, Design and characterization of orthotropic re-entrant auxetic structures made via EBM using Ti6Al4V and pure copper, Solid Free. Fabr. Symp 2011, pp. 464–474 , Austin, TX.
[9] P. Frigola, O.A. Harrysson, T.J. Horn, H.A. West, R.L. Aman, J.M. Rigsbee, D.A. Ramirez, L.E. Murr, F. Medina, R.B. Wicker, E. Rodriguez, Fabricating copper components with electron beam melting, Adv. Mater. Process. 172 (2014) 20–24.
[10] M.A. Lodes, R. Guschlbauer, C. Körner, Process development for the manufacturing of 99.94% pure copper via selective electron beam melting, Mater. Lett. 143 (2015) 298–301, https://doi.org/10.1016/j.matlet.2014.12.105.
[11] R. Guschlbauer, S. Momeni, F. Osmanlic, C. Körner, Process development of 99.95% pure copper processed via selective electron beam melting and its mechanical and physical properties, Mater. Charact. 143 (2018) 163–170, https://doi.org/10.1016/j.matchar.2018.04.009.
[12] Y. Bai, G. Wagner, C.B. Williams, Effect of particle size distribution on powder packing and sintering in binder jetting additive manufacturing of metals, J. Manuf. Sci. Eng. 139 (2017), 081019. https://doi.org/10.1115/1.4036640.
[13] Y. Bai, C.B. Williams, An exploration of binder jetting of copper, Rapid Prototyp. J. 21 (2015) 177–185, https://doi.org/10.1108/RPJ-12-2014-0180.
[14] A. Kumar, Y. Bai, A. Eklund, C.B. Williams, Effects of hot isostatic pressing on copper parts fabricated via binder jetting, Procedia Manuf, Elsevier B.V, Los Angeles, CA 2017, pp. 935–944, https://doi.org/10.1016/j.promfg.2017.07.084.
[15] A. Yegyan Kumar, Y. Bai, A. Eklund, C.B. Williams, The effects of hot isostatic pressing on parts fabricated by binder jetting additive manufacturing, Addit. Manuf. 24 (2018) 115–124, https://doi.org/10.1016/j.addma.2018.09.021.
[16] R.M. German, Powder Metallurgy Science, Second edition, 1994 (Princeton, NJ).
[17] R. Haynes, Effect of porosity content on ductility of sintered metals, Powder Metall. 20 (1977) 17–20.
[18] M.I. Aivazov, I.A. Domashnev, Influence of porosity on the conductivity of hot-pressed titanium-nitride specimens, Powder Metall. Met. Ceram. 7 (1968) 708–710, https://doi.org/10.1007/BF00773737.
[19] J.K. Carson, S.J. Lovatt, D.J. Tanner, A.C. Cleland, Thermal conductivity bounds for isotropic, porous materials, Int. J. Heat Mass Transf. 48 (2005) 2150–2158, https://doi.org/10.1016/j.ijheatmasstransfer.2004.12.032.
[20] J. Wang, J.K. Carson, M.F. North, D.J. Cleland, A new approach to modelling the effective thermal conductivity of heterogeneous materials, Int. J. Heat Mass Transf. 49 (2006) 3075–3083, https://doi.org/10.1016/j.ijheatmasstransfer.2006.02.007.
[21] C. Vincent, J.F. Silvain, J.M. Heintz, N. Chandra, Effect of porosity on the thermal conductivity of copper processed by powder metallurgy, J. Phys. Chem. Solids 73 (2012) 499–504, https://doi.org/10.1016/j.jpcs.2011.11.033.
[22] G.C.J. Bart, Thermal Conduction in Non Homogeneous and Phase Change Media, Technische Universiteit Delft, The Netherlands, 1994.
[23] B.C. Gundrum, D.G. Cahill, R.S. Averback, Thermal conductance of metal-metal interfaces, Phys. Rev. B - Condens. Matter Mater. Phys. 72 (2005), 245426. https://doi.org/10.1103/PhysRevB.72.245426.
[24] R.W. Powell, Correlation of metallic thermal and electrical conductivities for both solid and liquid phases, Int. J. Heat Mass Transf. 8 (1965) 1033–1045, https://doi.org/10.1016/0017-9310(65)90086-4.
[25] C.S. Smith, The relation between the thermal and electrical conductivities of copper alloys, Phys. Rev. 48 (1935) 166–167.
[26] F.H. Schofield, The thermal and electrical conductivities of some pure metals, Proc. R. Soc. London, Ser. A. 107 (1925) 206–227http://www.jstor.org/stable/94242.
[27] J.C.Y. Koh, A. Fortini, Prediction of thermal conductivity and electrical resistivity of porous metallic materials, Int. J. Heat Mass Transf. 16 (1973) 2013–2022, https://doi.org/10.1016/0017-9310(73)90104-X.
[28] S.J. Raab, R. Guschlbauer, M.A. Lodes, C. Körner, Thermal and electrical conductivity of 99.9% pure copper processed via selective electron beam melting, Adv. Eng. Mater. 18 (2016) 1661–1666, https://doi.org/10.1002/adem.201600078.
[29] ASTM B962-13, Standard Test Methods for Density of Compacted or Sintered Powder Metallurgy (PM) Products Using Archimedes' Principle, 2013https://doi.org/10.1520/B0962-13.
[30] ASTM E112-13, Standard Test Methods for Determining Average Grain Size, 2013https://doi.org/10.1520/E0112-13.1.4.
[31] S.A. Saltykov, Stereometric Metallurgy, Part 2, Armed Services Technical Information Agency, Arlington, VA, 1961.
[32] ASTM E8, Standard Test Methods for Tension Testing of Metallic Materials 1, ASTM. I, 2009 1–27, https://doi.org/10.1520/E0008_E0008M-13.
[33] ISO/ASTM 52921, Standard Terminology for Additive Manufacturing - Coordinate Systems and Test Methodologies, 2013https://doi.org/10.1520/ISOASTM52921-13.
[34] ASTM E1461, Standard Test Method for Thermal Diffusivity by the Flash Method, vol. i, ASTM, West Conshohocken, PA, 2013 1–11, https://doi.org/10.1520/E1461-13.
[35] Y. Bai, C. B. Williams, The effect of inkjetted nanoparticles on metal part properties in binder jetting additive manufacturing," Nanotechnol. 29(39), p. 395706. doi: https://doi.org/10.1088/1361-6528/aad0bb.
[36] S.A. Lurie, Y.O. Solyaev, L.N. Rabinskiy, P.O. Polyakov, I. Sevostianov, Mechanical behavior of porous Si3N4 ceramics manufactured with 3D printing technology, J. Mater. Sci. 53 (2018) 4796–4805, https://doi.org/10.1007/s10853-017-1881-0.
[37] I. Sevostianov, J. Kováčik, F. Simančík, Elastic and electric properties of closed-cell aluminum foams: cross-property connection, J. Mater. Sci. Eng. A 420 (2006) 87–99, https://doi.org/10.1016/j.msea.2006.01.064.
[38] JC Maxwell, A Treatise on Electricity and Magnetism (Vol. vol. 1), 1873, Oxford: Clarendon Press.
[39] I. Sevostianov, A. Giraud, Generalization of Maxwell homogenization scheme for elastic material containing inhomogeneities of diverse shape, Int. J. Eng. Sci. 64 (2013) 23–36, https://doi.org/10.1016/j.ijengsci.2012.12.004.
[40] T. Mori, K. Tanaka, Average stress in matrix and average elastic energy of materials with misfitting inclusions, Acta Metall. 21 (1973) 571–574, https://doi.org/10.1016/0001-6160(73)90064-3.